Electronic Supplementary Information

Monolithic 3D-Printed Split-and-Recombine Micromixer Integrated into a Microfluidic Concentration Gradient Generator

Francisco Navarro Molina[a], Jitendra Paliwal[b], Elham Salimi[*a]

a. Department of Electrical and Computer Engineering, University of Manitoba, Winnipeg, Canada.
b. Department of Biosystems Engineering, University of Manitoba, Winnipeg, Canada.

Keywords

3D printing; stereolithography (SLA-DLP); split-and-recombine micromixer; concentration gradient generator; microfluidics; lab-on-a-chip.

Corresponding Author

*Tel.: +1-(204)-474-6419. Email: elham.salimi@umanitoba.ca

S1. Theoretical Simulations Parameters

Theoretical simulations were conducted using COMSOL Multiphysics 6.2 to both qualitatively visualize and quantitatively determine the mixing efficiency and outlet concentration distribution in the SAR micromixer and the MCGG. The SolidWorks CAD models of each device were imported into COMSOL, and a negative solid geometry was generated to define the internal microchannel domains. Each device was simulated in a separate file to perform an independent study. A physics-controlled mesh with a *fine* element size was applied to each model. The two inlet faces of each device were defined as the fluid boundary conditions, corresponding to the inlet microchannels where the individual fluid streams entered the mixing region.

At the inlets, steady laminar flow conditions were applied with equal flow rates and inlet concentrations of 0 and 1 mol/m^3. No-slip boundary conditions were imposed along all channel walls. The working fluid was modeled as water (ρ = 997 kg·m^{-3}, μ = 0.001 Pa·s). The Laminar Flow and Transport of Diluted Species physics interfaces were coupled to simultaneously solve for the velocity field and species concentration. A steady-state solver was used to obtain converged solutions for the flow and concentration distributions.

For the SAR micromixer a parametric sweep was performed across Reynolds numbers (Re = [0.1, 0.5, 1, 5, 10, 30, 50, 100]) and diffusion coefficients (D = 1 x 10^{-9} and 9.33 x 10^{-11} m^2/s) to represent solutes of different molecular diffusivities. The computed concentration fields were post-processed to evaluate the local and average mixing efficiencies (ME) along the microchannel using Equation (2) from the main text.

The calculated parameters used for the SAR micromixer simulations are listed in Table S1.

Table S1. Calculated inlet velocities and flow rates corresponding to simulated Reynolds numbers.

Reynolds number (Re)	Inlet velocity (mm/s)	Flow rate (µL/min)
0.1	0.167	1.81
0.5	0.836	9.03
1.0	1.672	18.05
5.0	8.358	90.27
10.0	16.717	180.54
30.0	50.151	541.62
50.0	83.584	902.71
100.0	167.170	1805.42

S2. Summary of 3D printing Settings

Table S2. 3D Printing settings

Settings Printer (CADWorks3D)	**SAR micromixer** Profluidics 285D	**MCGG** Profluidics 285D
Resin volume (mL)	6.82	6.90
Layer height	30 µm	From 0 to 2.1 mm [50 µm], from 2.1 to 3 mm [30 µm], and from 3 to 11.55 mm [50 µm]
Base layers	1	1
Base exposure (s)	30.00	30.00
Buffer layers	2	2
Power (%)	100	100
Exposure time (s)	0.8	0.8 and 1 [30 µm, and 50 µm]
Anti-aliasing	Yes	Yes
Total print time [min]	~76	~140
Post-curing time [sec]	30	30

Regarding the vertical resolution, while the printer supports a minimum slicing thickness of 5 µm, we utilized layer heights of 30-50 µm. This choice was made to balance fabrication speed with structural quality. Specifically, thinner layers significantly increase the number of light exposure cycles, which can lead to cumulative "dark polymerization" or parasitic light leakage. This phenomenon effectively reduces the accuracy of enclosed voids and increases the likelihood of clogging in the 150 µm SAR constrictions. Furthermore, reducing the layer thickness to 5 µm would not substantially reduce dead volume, as dead volume is primarily dictated by the channels XY geometry and the 150 µm minimum feature constraint required for reliable resin extraction.

S3. Confocal Laser Scanning Microscopy Settings

Fluorescence imaging of mixing performance was conducted using a Zeiss LSM 700 Axio Imager 2 confocal laser scanning microscope equipped with a Plan-Apochromat 10×/0.45 M27 objective. Image acquisition was performed in line sequential mode under fluorescence contrast with the following parameters:

- Excitation wavelength: 488 nm (FITC channel)
- Emission detection range: 493–800 nm
- Detection channels: Channel 1 (FITC fluorescence) and transmitted PMT (brightfield)
- Detector type: Photomultiplier tube (PMT)
- Detector gain: 676.2 (FITC), 168.9 (transmitted)
- Pinhole size: 2.19 Airy units
- Pixel size: 1.25 µm × 1.25 µm × 2.00 µm
- Image resolution: 512 × 512 pixels
- Bit depth: 12-bit
- Z-stack: 207 slices (total depth = 412 µm)
- Depth of focus: 5.43 µm
- Scan speed: Pixel time 3.15 µs, line time 30 µs, frame time 1.94 s
- Averaging: 1 (unidirectional scan direction)
- Numerical aperture (NA): 0.45
- Laser power (488 nm): 10.0%
- Zoom: 1.0×

All images were acquired with identical microscope settings to maintain comparable fluorescence intensity values across samples. Raw 12-bit images were converted to grayscale and analyzed in Python 3.13.2 following the image processing workflow described in Section 2.4 of the main text.

S4. SAR Design Measurements

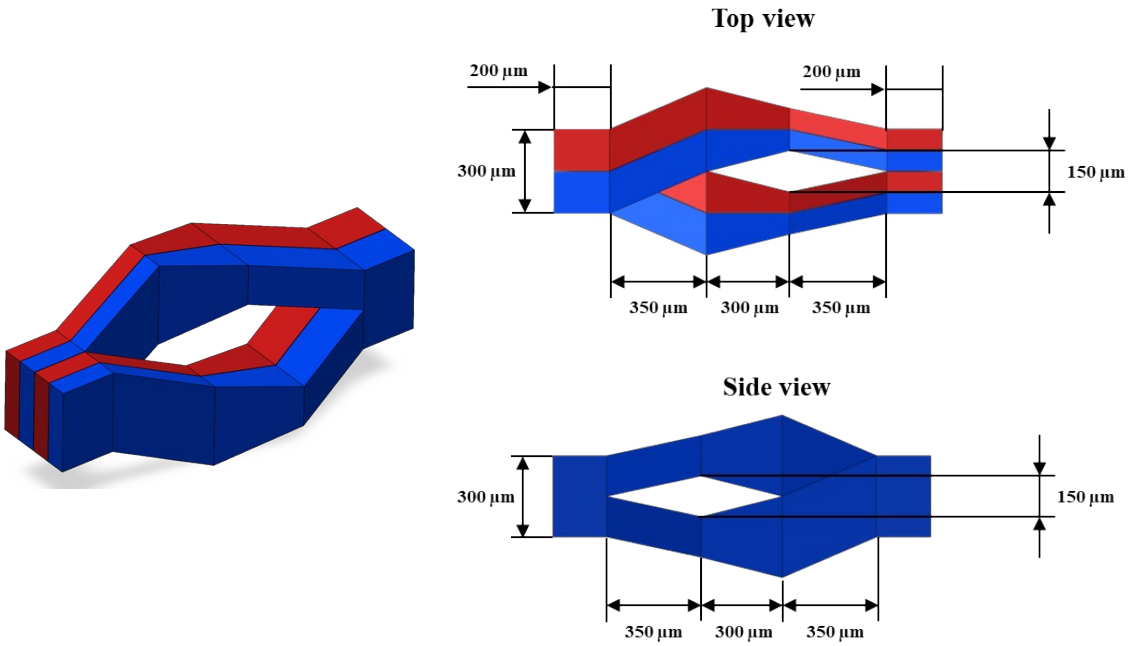

Fig. S1. Design of single SAR unit. The microfluidic channel dimensions are 300 x 300 µm^2. The split and recombination section have an axial length of 350 µm, 300 µm, 350 µm. The distance between SAR units is 200 µm meaning the total axial length for each unit is 1.2 mm.

S5. Design Optimization

To identify the optimal split-and-recombine (SAR) architecture for monolithic SLA DLP fabrication, a systematic study was conducted to determine optimal design parameters to satisfy manufacturability and performance. In addition to the number of mixing units, which is discussed in detail in the manuscript, we considered four primary design aspects: a) dimensions, b) lateral offset, c) orientation, and d) transition section geometry.

a) Dimensions and Printability:

The internal dimensions of microfluidic channels are restricted by the printer and resin properties as well as the post-print cleaning process. While the printer's XY resolution is 40 µm, enclosed channels are prone to over-curing or clogging due to trapped resin.

As shown in Table S3, we determined that a minimum channel dimension of 150 µm is required for reliable and reproducible fabrication. Below this threshold, the post-print cleaning procedure was insufficient to clear the channels.

Table S3. Manufacturability of enclosed SAR channels.

Nominal Dimension (µm)	Successful Clearing?	Observation
80	No	Consistent clogging; resin solidified in narrow transitional sections of SAR units.
100	No	Occasional clogging; resin solidified in narrow transitional sections of SAR units .
150	Yes	Easy to clear, no visible internal defects.
200	Yes	Easy to clear, no visible internal defects.
300	Yes	Easy to clear, no visible internal defects.

b) Lateral Offset (α):

The basic SAR unit was parameterized with a variable α, representing the lateral offset of the splitting junctions (Fig. S2). This parameter is critical for structural reliability of the internal geometry. At $\alpha = 0$ º, the device footprint is minimized, and the mixing performance is less influenced by lateral centrifugal forces, resulting in a more predictable SAR flow pattern, particularly at higher Reynolds numbers. However, the V-shaped structure formed at the channel split/recombine junctions creates a thin separating interface. In our printing attempts, this interface frequently failed to form properly, resulting in the unintended merging of the two distinct channels into a single channel. Based on several printing trials, we selected a lateral angle of $\alpha = 46°$ (corresponding to a full channel width of 150 µm between the splitting branches; Fig. S1) to ensure reliable and reproducible fabrication.

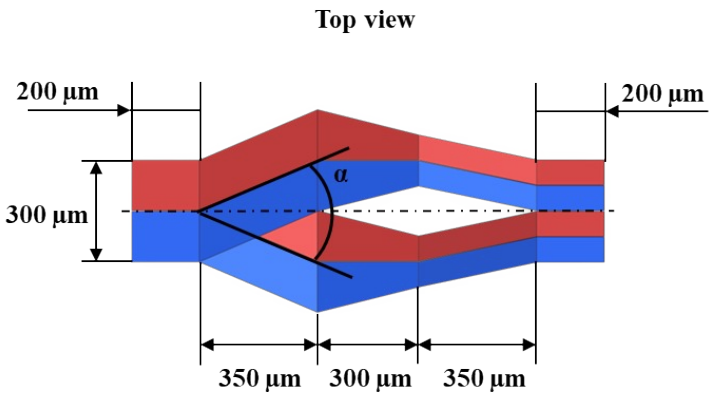

Fig. S2. Top view of proposed designed with variable parameter α.

c) Orientation:

We compared two geometric orientations for the SAR units: unidirectional (where the splitting shift occurs in the same direction for each subsequent unit) and alternating (where the direction of the split flips 180° at each stage).

As shown in the ME vs *Re* analysis (Fig. S3) unidirectional designs consistently outperformed alternating designs. The unidirectional shift induces a consistent rotational component to the flow, which enhances the split-and-recombine mechanism at higher *Re*. Conversely, the alternating design tends to "undo" the lateral displacement from the previous stage, slowing the homogenization process and resulting in a lower ME for the same number of stages.

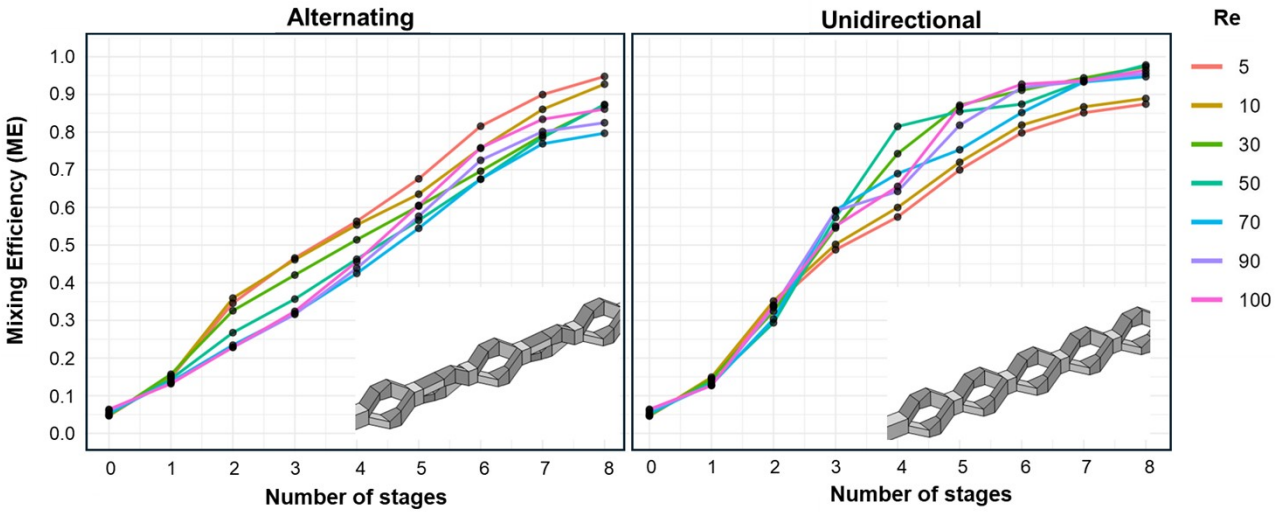

Fig. S3. Mixing efficiency versus number of stages for all Reynolds number tested for alternating and unidirectional orientations of the SAR units.

d) Geometry:

Finally, we evaluated the impact of transition sections shape: smooth curves versus

trapezoidal/straight sections. Curved transitions utilize smooth tapering to guide the flow from split to recombine junctions. While curved transitions are easier to clear of uncured resin, simulation data (Fig. S4) shows that in curved transitions the boundary between recombined streams are significantly inclined which interferes with the SAR mixing mechanism. While the curved structures can increase the mixing efficiency at higher *Re* (due to higher centrifugal forces), they drastically reduce the mixing efficiency at *Re* < 10 (Fig. S5).

Following this systematic study, the trapezoidal/straight, unidirectional, with α = 46 º was selected as the optimal architecture for 3D printing.

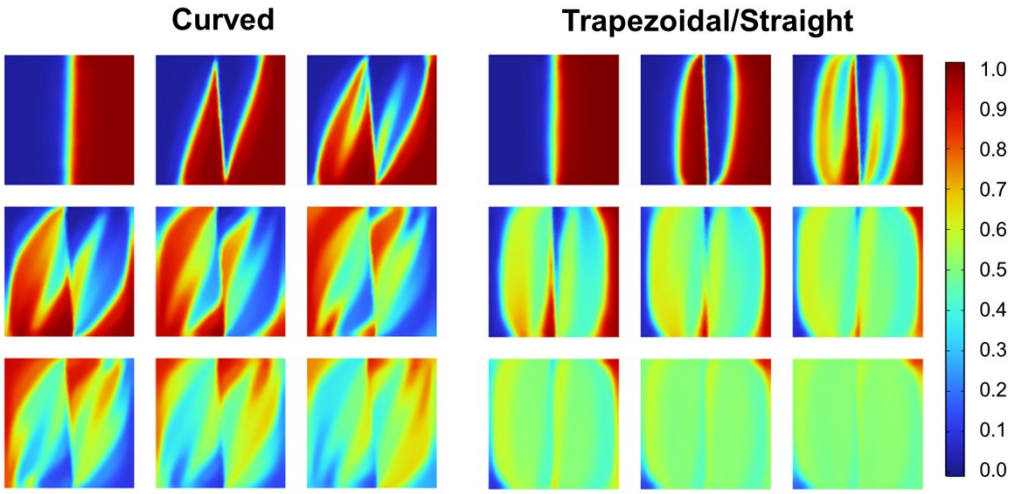

Fig. S4. Simulated cross-sections of the geometries analyzed for *Re* = 5, showcasing the difference between a tapered geometry and straight transitions.

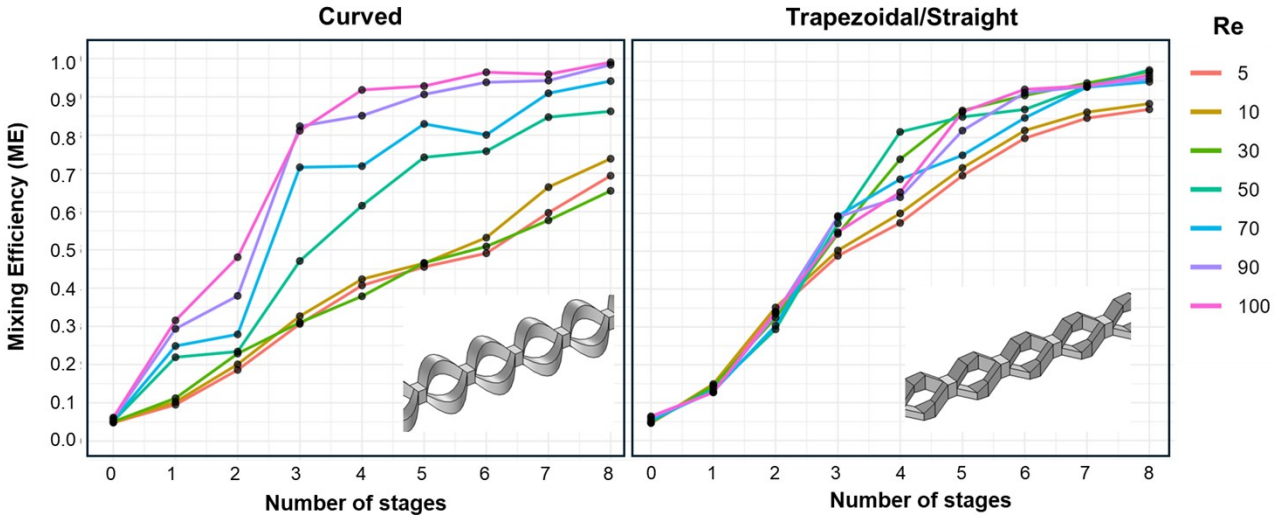

Fig. S5. Mixing efficiency versus number of stages for all Reynolds number tested tapered and trapezoidal transitions.

S6. MCGG Electrical Analogy Design

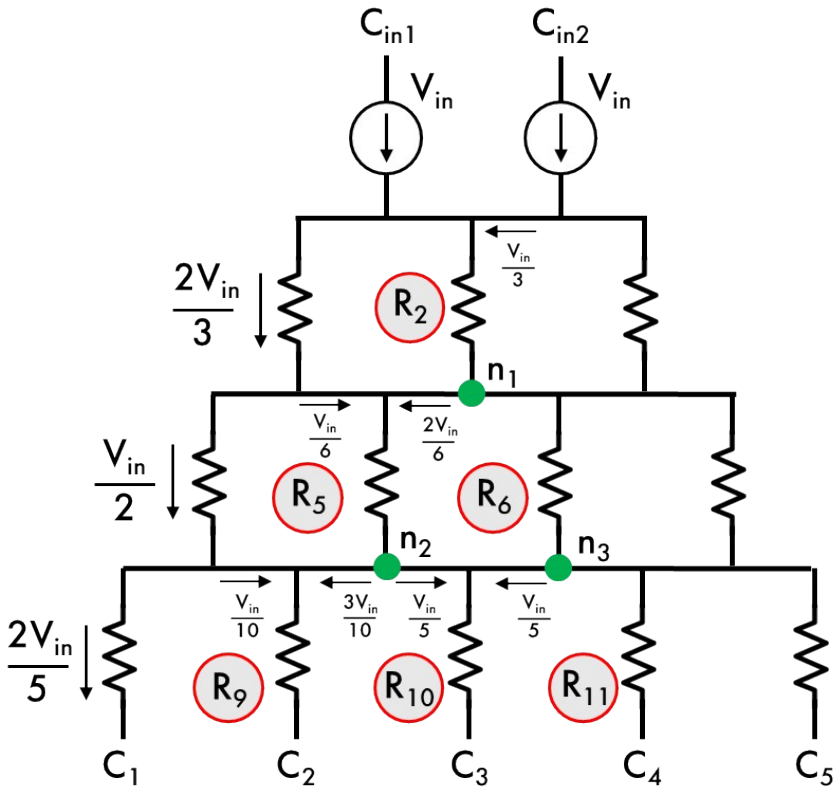

Fig. S6. Each microchannel segment is represented as a hydraulic resistor (Ri), where the pressure drop across the channel (ΔP) is analogous the voltage drop (V) in an electric circuit, and the volumetric flow rate (Q) corresponds to the electric current (I). The network obeys Kirchhoff's current and voltage laws, allowing calculation of flow distribution and concentration ratios (C1−C5) throughput the gradient generator.

The gradient generator was based on a resistor-inspired tree-like network. By splitting and recombining streams through balanced channel resistances, the MCGG produces predictable dilution ratios. The flow distribution through each branch can be modeled using the electrical circuit analogy. The Hagen-Poiseuille law for laminar flow,

$$\Delta P = QR_h \tag{1}$$

is formally equivalent to Ohm's law,

$$V = IR \tag{2}$$

Where pressure drop (ΔP) is equivalent to the voltage (V), volumetric flow rate (Q) is the current (I), and hydraulic resistance (R_h) is the resistance (R). Each node in the microfluidic network obeys the same conservation laws as an electrical circuit:

$$\sum Q_{in} = \sum Q_{out} \tag{3}$$

By assigning flow resistances (R_h) to each channel and pressures (P_i) at the nodes, the system can be solved algebraically for all flow rates (Q_i) using Kirchoff's laws. For a simplified three-level "Christmas tree" gradient generator with resistances R_1 to R_{12} as shown in Fig. S6, at a node connecting multiple downstream channels, the flow rate is distributed inversely to the hydraulic resistance of each branch:

$$Q_1 = Q_T \frac{R_1}{R_1 + R_2} \tag{4}$$

$$Q_2 = Q_T \frac{R_2}{R_1 + R_2} \tag{5}$$

Where Q_T is the total incoming flow and R_1, R_2 are the downstream resistances. This relationship is equivalent to the current division rule in electrical circuits and ensures pressure continuity across nodes.

At each mixing junction, the concentration of solute exiting the node is determined by the weighted average of inlet concentrations (C_1, C_2) based on their respective flow rates:

$$C_R = \frac{Q_1 C_1 + Q_2 C_2}{Q_1 + Q_2} \tag{6}$$

Substituting the flowrate expressions from above yields:

$$C_R = \frac{C_1/R_1 + C_2/R_2}{1/R_1 + 1/R_2} \tag{7}$$

This equation is formally equivalent to the voltage division law in electrical circuits and allows direct prediction of outlet concentrations at each node of the gradient generator.

Table S4 summarizes the theoretical concentration distribution obtained from the electrical-hydraulic analogy for a three-level "Christmas tree" gradient generator with equal branch resistances.

Table S4. Calculated relative concentrations at mixing nodes and outlets of the microfluidic gradient generator.

Node/Outlet	Mixing Streams	Equation Used	Concentration (C)
C_{in1}	-	-	0.00
C_{in2}	-	-	1.00
n_1	C_{in1},C_{in2}	$C_{R2} = (0 + (1/3)C_{in2})/(2/3)$	0.50
n_2	C_{in1},n_1	$C_{R5} = (0 + (2/6)n_1)/(0.5)$	0.33
n_3	n_1,C_{in2}	$C_{R6} = ((1/6)C_{in2} + (2/6)n_1)/(0.5)$	0.66
C_1	From C_{in1}	-	0.00
C_2	C_{in1},n_2	$C_2 = (0 + (3/10)n_2)/(0.4)$	0.25
C_3	n_2, n_3	$C_3 = ((1/5)n_2 + (1/5)n_3)/(0.4)$	0.50
C_4	n_3,C_{in2}	$C_4 = ((3/10)n_3 + (1/10)1)/(0.4)$	0.75
C_5	From C_{in2}	-	1.00

S7. Simulation of Pressure Values.

Since the experimental setup utilized a flow-rate driven syringe pump, the internal pressure conditions could not be measured directly during operation. To establish these values, numerical simulations were performed using COMSOL Multiphysics 6.2. The stationary Laminar Flow physics interface was used to compute the pressure distribution across the SAR-MCGG domain.

The results, summarized in Table S5, indicate that the total pressure drop across the device did not exceed approximately 7.5 kPa even at the maximum experimental flow rate (*Re* = 100).

Table S5. Simulated total pressure drop across the SAR micromixer and MCGG.

Reynolds number (Re)	Total Flow Rate (Q, µL/min)	Simulated ΔP (Pa) for the SAR micromixer	Simulated ΔP (Pa) for the MCGG
0.1	1.81	6.64	2.24
0.5	9.03	33.23	11.22
1	18.05	66.49	22.44
5	90.27	333.15	112.46
10	180.54	668.87	225.59
30	541.62	2052.7	686.34
50	902.71	3515.2	1163.0
100	1805.42	7561.5	2443.0